Corrosion Science 170 (2020) 108657

Contents lists available at ScienceDirect

Corrosion Science

journal homepage: www.elsevier.com/locate/corsci

Anisotropic corrosion behavior of Sc and Zr modified Al-Mg alloy produced by selective laser melting

Dongdong Gu[a,b,*], Han Zhang[a,b], Donghua Dai[a,b], Chenglong Ma[a,b], Hongmei Zhang[a,b], Yuxin Li[a,b], Shuhui Li[c]

[a] College of Materials Science and Technology, Nanjing University of Aeronautics and Astronautics, Yudao Street 29, Nanjing 210016, Jiangsu Province, PR China
[b] Jiangsu Provincial Engineering Laboratory for Laser Additive Manufacturing of High-Performance Metallic Components, Nanjing University of Aeronautics and Astronautics, Yudao Street 29, Nanjing 210016, Jiangsu Province, PR China
[c] Shanghai Key Laboratory of Digital Manufacture for Thin-Walled Structures, Shanghai Jiao Tong University, 200240, Shanghai, PR China

ARTICLE INFO

Keywords:
Additive manufacturing
Selective laser melting
Al-Mg-Sc-Zr
corrosion behavior
Microstructure

ABSTRACT

Electrochemical measurements and microstructural analyses were conducted to investigate the corrosion behaviors on different planes of Sc and Zr modified Al-Mg alloy produced by selective laser melting (SLM). Results indicated that the XY-plane exhibited a superior corrosion resistance with a lower current density (i_{corr} = 57.1 μA cm^{-2}) compared to the XZ-plane in 3.5 wt.% NaCl solution at room temperature. The microstructural analyses suggested that the anisotropic corrosion resistances of the SLM produced Al-Mg-Sc-Zr alloy related to the quite different microstructures on different planes, which included the molten pool boundary density, Al_3(Sc,Zr) precipitation distribution, grain size distribution, and crystallographic orientation.

1. Introduction

With the development of aerospace and automotive industries, there is a strong demand for lightweight and high-performance components with complex structures. Due to the excellent properties of low density, high strength to weight ratio and acceptable corrosion resistance, aluminum alloys especially high-performance aluminum alloys are suitable candidates. For conventional processing methods, aluminum alloys are fabricated by casting, forging and plastic deformation, which are not suitable for processing components with complex geometries. Selective laser melting (SLM), as one of the developed Additive Manufacturing (AM) techniques, has been widely used in fabricating metallic parts in recent years [1–3]. It is able to produce components with complex structures by selectively melting successive powder layers using a high intensity laser beam controlled by a computer. SLM provides plenty of advantages including high geometrical freedom, high production flexibility and less material waste [4–8].

So far, SLM has been used in fabricating Al alloys, but mainly concentrate on 4xxx Al-Si alloys, including AlSi12, AlSi10Mg and AlSi7Mg [9,10]. These Al alloys are casting alloys with a good wedability, thus are suitable for the SLM process. However, the mechanical properties of these SLM produced Al-Si alloys are limited (normally below 400 MPa), which are difficult to meet the needs for the aerospace industry. Therefore, there is a strong demand to develop high-performance Al alloys which could be produced by SLM, such as 2xxx Al-Cu, 6xxx Al-Mg-Si and 7xxx Al-Zn-Mg alloys. However, these alloys exhibit poor processabilities during the SLM process due to their relatively large freezing ranges, which lead to hot cracks and low mechanical properties [11–13]. A good alternative for these high-performance Al alloys is Sc and Zr modified Al-Mg alloy. Al-Mg alloys are widely applied in aerospace and ships due to their good corrosion resistance, admirable weld ability and moderate strength. An addition of a small quantity of Sc and Zr to Al-Mg alloys can significantly refine grains and form a high density of nano-sized Al_3(Sc,Zr) precipitations, leading to a prominent enhancement of mechanical properties and thermal stabilities [14,15].

Recent works have reported a good processability of Al-Mg-Sc-Zr alloy for the SLM process [16–18]. A high strength (~520 MPa) combined with a good ductility (~12%) can be achieved for the SLM produced Al-Mg-Sc-Zr alloy after heat treatment, showing excellent compatibility between the SLM process and the Al-Mg-Sc-Zr alloy [19]. Spierings et al. [20] reported the microstructure of the SLM produced Al-Mg-Sc-Zr alloy, which consisted of fine grained areas distributed along molten pool boundaries and coarser grained regions formed inside the molten pool. Li et al. [21] investigated the influence of heat treatment on microstructure and mechanical properties, showing the

* Corresponding author.
E-mail address: dongdonggu@nuaa.edu.cn (D. Gu).

https://doi.org/10.1016/j.corsci.2020.108657
Received 27 December 2019; Received in revised form 8 March 2020; Accepted 6 April 2020
Available online 15 April 2020
0010-938X/

strength and ductility trade-off can be controlled by optimizing aging parameters. Schmidke et al. [22] further studied the mechanical properties of heat treated Al-Mg-Sc-Zr specimens along 0°, 45° and 90° directions, and found tensile strengths more than 520 MPa were obtained for all directions, showing low anisotropy in mechanical properties. The densification behavior, microstructure evolution and mechanical properties of the SLM produced Al-Mg-Sc-Zr alloy were fully studied in recent works, but there is still a lack of works focusing on its corrosion behavior. While the corrosion resistance of SLM produced Al-Mg-Sc-Zr components could be a key factor to influence its engineering applications. In addition, it is interesting to note that SLM produced parts exhibit different microstructures on different planes due to the layer-by-layer manufacturing characteristics of the SLM process. Thus the corrosion resistances on different planes of SLM produced parts could be different. Dai et al. [23] studied the corrosion behaviors on different planes of Ti-6Al-4 V alloy processed by SLM, and indicated a better corrosion resistance for the building plane compared to building direction plane. This anisotropic corrosion resistance for SLM produced Ti-6Al-4 V was attributed to the different microstructures on different planes. Although the isotropic mechanical properties of SLM produced Al-Mg-Sc-Zr alloy has been confirmed, the corrosion behaviors on different planes are still unclear. A better understanding of the corrosion behavior of the SLM produced Al-Mg-Sc-Zr alloy will further facilitate its design and application. Therefore, it is of great significance of bridging the knowledge gap for the corrosion behaviors of SLM produced Al-Mg-Sc-Zr alloy on different planes.

The aim of this work is to investigate the corrosion behaviors on different planes (i.e. the building plane, XY-plane; the building direction plane, XZ-plane) of the SLM processed Al-Mg-Sc-Zr alloy. Electrochemical measurements including open circuit potential (OCP), potentiodynamic polarization and electrochemical impedance spectroscopy (EIS) tests were conducted to study the corrosion behaviors of SLM produced Al-Mg-Sc-Zr alloy. Microstructures were investigated by electron back scattered diffraction (EBSD) and scanning electron microscopy (SEM). Passive film compositions were qualitatively analyzed by X-ray photoelectron spectroscopy (XPS). Finally, the mechanisms for the corrosion behaviors on different planes of the SLM produced Al-Mg-Sc-Zr alloy were systematically analyzed and summarized.

2. Experimental

2.1. Materials and solution preparation

Al-Mg-Sc-Zr specimens with a dimension of 10 mm × 10 mm × 10 mm were produced by SLM. Gas-atomized powder with a chemical composition of Al-4.2Mg-0.4Sc-0.2 Zr was applied in this study. Morphologies of the initial powder are shown in Fig. 1a, and the particle size distribution of the initial powder is further provided in Fig. 1b. Particle size d_{50} of the starting powder was 27.8 μm and d_{90} was 38.9 μm. Before the SLM process, the initial powder was dried in vacuum for 10 h at 150 ℃ to improve its flowability. The SLM process was performed using an SLM-150 machine. This equipment has a 500 W Yb: YAG fiber laser with a spot size of 70 μm. A high purity argon atmosphere with oxygen content less than 50 ppm was maintained during the SLM process. Laser power, layer thickness, laser scan speed and hatch spacing were fixed at 400 W, 30 μm, 600 mm/s and 60 μm, respectively. Before Al-Mg-Sc-Zr specimens were to be processed, an Al substrate was fixed on the platform. A thin layer of Al-Mg-Sc-Zr powder with a thickness of 30 μm was then deposited on the substrate by powder coating scraper. Then, the laser beam scanned the powder bed according to the CAD model. Substrate pre-heating was not applied and the specimen was scanned using an island scanning strategy with a 37° rotation between two neighboring layers. Different planes of the SLM produced Al-Mg-Sc-Zr specimen investigated in this work are shown in Fig. 1c, where XY-plane represents the building plane and XZ-plane represents the building direction plane. The SLM produced Al-Mg-Sc-Zr specimen is shown in Fig. 1d. The relative density of this specimen was higher than 99.5%, which was tested by Archimedes method. A post heat-treatment of 325℃ for 4 h was performed to this specimen in argon atmosphere [24]. Generally, the properties of rare earth modified aluminum alloys, especially lightweight and high strength, have important application prospects in the aerospace field. However, due to its special marine service environment, shipborne aircraft are required to have good corrosion resistance while having good mechanical properties. In this paper, NaCl solution was selected as the corrosion solvent to simulate the marine corrosive environment. A 3.5 wt.% NaCl solution for electrochemical measurements was prepared by deionized water and analytical grade reagents.

2.2. Electrochemical measurements

Before electrochemical measurements, the studied planes of the SLM produced Al-Mg-Sc-Zr specimen were mechanically abraded up to 5000-grit by SiC paper and then polished with water-based diamond suspensions. Electrochemical tests were performed in 3.5 wt.% NaCl solution at room temperature using an electrochemical workstation (CHI660e, ChenHua, China). A conventional three-electrode cell system was used, which consisted of a platinum foil acted as a counter electrode, a saturated calomel electrode (SCE) acted as a reference electrode and the studied plane of the specimen acted as a working electrode. Open circuit potential, electrochemical impedance spectroscopy and potentiodynamic polarization tests were performed in this study. Before EIS and polarization measurements, the tested surfaces were immersed in the NaCl solution for enough time to obtain a stable OCP value. The EIS tests were performed under a stabilized potential and the frequency was ranged from 10^{-2} to 10^{5} Hz with an amplitude of 10 mV. The potentiodynamic polarization curves were tested from -0.4 V to -1.7 V under a scanning rate of 2 mV/s. All electrochemical measurements were tested for three times for data reproducibility.

2.3. Characterizations

Before microstructure characterization, the studied surfaces of the SLM produced Al-Mg-Sc-Zr specimen were ground and polished. Then a Keller`s reagent was applied to etch the surfaces. The microstructures and corrosion morphologies were performed using an optical microscopy (OM, Olympus Corporation, Japan) and a Scanning electron microscopy (SEM, Hitachi, Japan). Electron back-scattered diffraction (EBSD) tests were performed by a NANO SEM 430 machine (FEI, Hillsboro, Oregon) with a scanning step size of 0.1 μm. Chemical compositions of the passive film were characterized by X-ray photo electron spectroscopy (XPS) using a 250XI equipment. Before the XPS test, the tested surface of the sample was polished and ultrasonically cleaned. Then the sample was immersed in the 3.5 wt.% NaCl solution and its open-circuit potential was measured. After the open-circuit potential of the sample reached a stable value for 10 hours, the XPS analysis was performed to conduct the compositions of the passive film formed on the surface.

3. Results

3.1. Characterization of microstructure

Fig. 2 shows the microstructure of the SLM produced Al-Mg-Sc-Zr specimen. Based on the three-dimensional optical metallographic image shown in Fig. 2a, quite different microstructures were obtained for the XY- and XZ-planes. Massive molten pool boundaries with arc shapes were formed on the cross section (XZ-plane) owing to the layer-by-layer manufacturing process. While sparse molten boundaries with straight-line shapes were generated on the top surface (XY-plane) due to the track-by-track building process. Thus the molten pool boundary density on the XZ-plane was much higher than that of the XY-plane. Fig. 2b

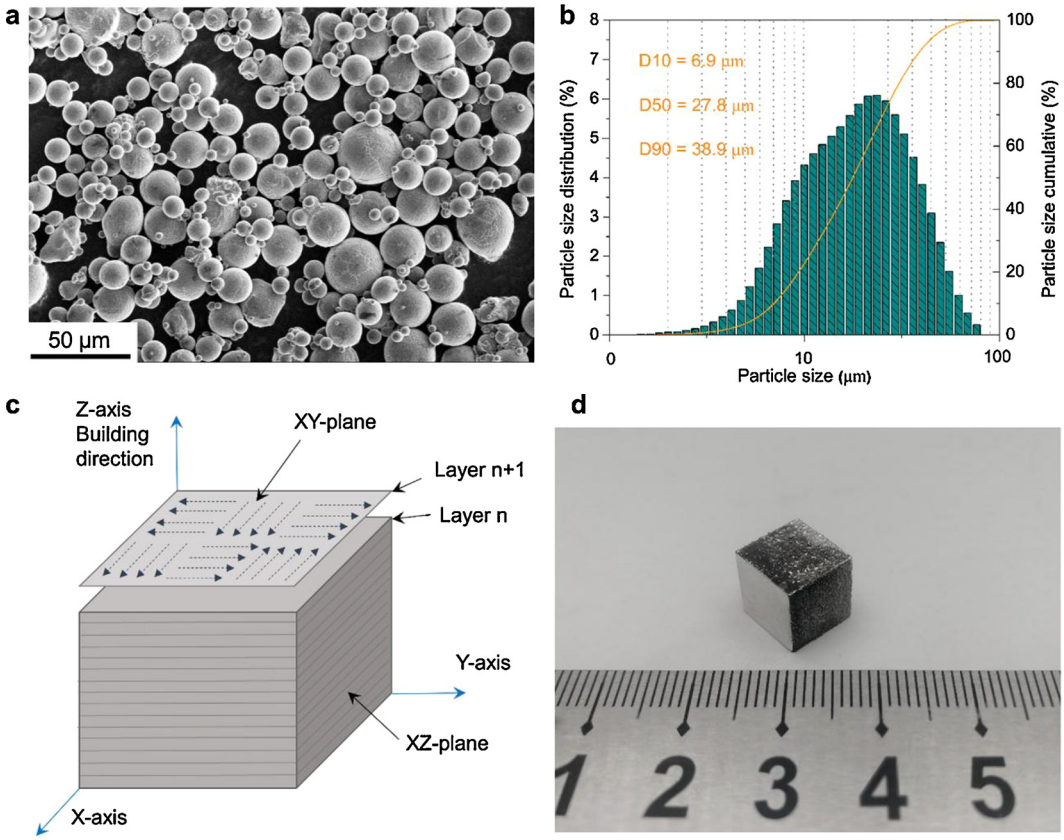

Fig. 1. (a) SEM image of initial Al-Mg-Sc-Zr powder. (b) Particle size distribution of initial Al-Mg-Sc-Zr powder. (c) Schematic of the XY- and XZ-planes of SLM produced Al-Mg-Sc-Zr alloy and the island scanning strategy of laser beam. (d) SLM produced Al-Mg-Sc-Zr specimen with a dimension of 10 mm × 10 mm × 10 mm.

shows a backscatter SEM micrograph of the XZ-plane of the Al-Mg-Sc-Zr specimen fabricated by SLM. Large and elongated grains with an average length of 20 μm were evident in the center of the molten pool. Fine and equiaxed grains with mean size below 2 μm were formed along the molten pool boundaries. It is obvious that plenty of precipitations were generated in α-Al matrix, where white particles related to $Al_3(Sc,Zr)$ precipitations and dark particles related to Al-Mg oxides [25]. These precipitations were preferentially generated in the fine grain area along the molten pool boundaries. Only limited particles formed along grain boundaries in the coarsen area. Similar microstructure characteristic of SLM produced Al-Mg-Sc-Zr specimen was also observed by Spierings [20] and Shi [26].

EBSD images of grain boundaries for the XZ- and XY-planes of the SLM produced Al-Mg-Sc-Zr specimen are presented in Fig. 3a and b, respectively. In these figures, red lines represent low angle grain boundaries (LAGBs) ($2^\circ \leq \theta \leq 15^\circ$) and dark lines represent high angle grain boundaries (HAGBs) ($\theta \geq 15^\circ$). Grain features for the XZ- and XY-planes of the SLM produced Al-Mg-Sc-Zr specimen were significantly different. It can be observed that massive and equiaxed grains with mean size below 2 μm combined with columnar grains with mean size about 10 ~ 15 μm were formed on the XZ-plane (Fig. 3a). While Fig. 3b revealed that cellular grains with mean size about 3 ~ 5 μm were generated on the XY-plane. Quantitative data of EBSD measurements on the XY- and XZ-planes of the SLM produced Al-Mg-Sc-Zr specimen are

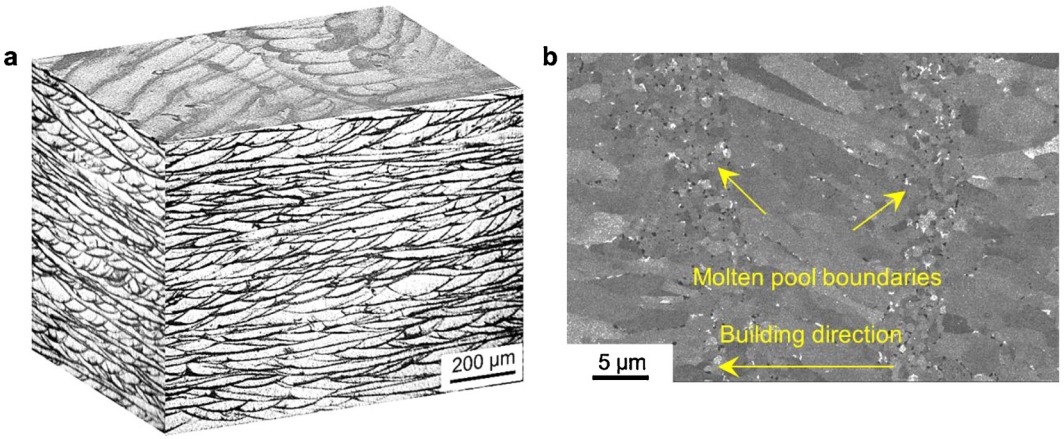

Fig. 2. (a) 3D optical metallographic image of SLM produced Al-Mg-Sc-Zr specimen, showing the different microstructures on different planes. (b) Backscatter SEM micrograph of the XZ plane of SLM produced Al-Mg-Sc-Zr specimen after heat treated at 325℃ for 4 h, showing the precipitates were preferred generating along molten pool boundaries.

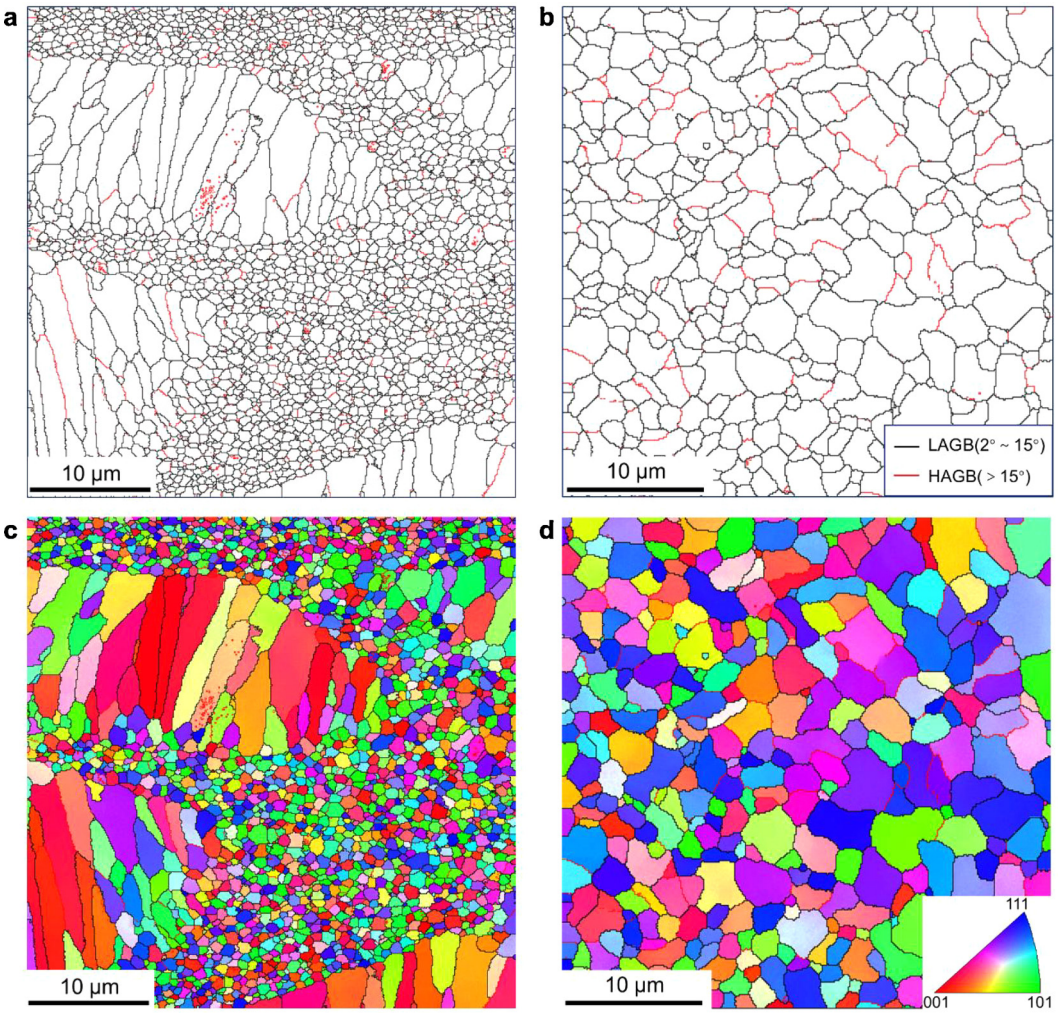

Fig. 3. EBSD results of XY- and XZ-planes of SLM produced Al-Mg-Sc-Zr specimen, showing different grain size distributions. (a) and (b) are grain boundary maps of XZ- and XY-planes with distinguished grain boundaries (black line represents low angle grain boundary and red line represents high angle grain boundary). (c) and (d) are the EBSD inverse pole figure (IPF) maps of XZ- and XY-planes of SLM produced Al-Mg-Sc-Zr specimen, respectively.

Table 1
EBSD results of the XY- and XZ-planes of SLM produced Al-Mg-Sc-Zr specimen.

Parameters	XY-plane	XZ-plane
Number of grains	281	1955
Average grain size (μm)	2.17	0.87
Total length of grain boundary (mm)	1.61	4.34
Grain boundary density (mm^{-1})	15.87	26.72
Fraction of LAGBs (%)	14.4	8.5

summarized in Table 1. The average grain size of the XY-plane was significantly higher than that of the XZ-plane, which were 2.17 μm and 0.87 μm, respectively. Due to the refined grain size, the grain boundary density of the XZ-plane was 26.72 mm^{-1}, much higher than 15.87 mm^{-1} of the XY-plane. The grain size distributions on the XZ- and XY-planes of the Al-Mg-Sc-Zr specimen fabricated by SLM are further provided in Fig. 4. Most grains on the XZ-plane were around 1 μm while the grain size on the XY-plane was more uniformly distributed below 5 μm. From an area fraction point of view, the grain size distribution on the XZ-plane showed a bimodal pattern, which consisted of fine grains with size below 2 μm and coarse grains with size above 4 μm. This bimodal microstructure was related to the fine grain area formed along molten pool boundaries and coarse grain region formed in the molten pool centers as observed in Fig. 3a. As for the XY-plane, the grain size was evenly distributed and no apparent bimodal distribution can be identified (Fig. 4d).

The distributions of grain boundary misorientation angles on the XZ- and XY-planes are shown in Fig. 5. The black column is McKenzie plot [27], which represents a random or theoretical distribution of grain misorientation. Compared to the XY-plane, the misorientation angle distribution on the XZ-plane was more closed to a random distribution. This is probably related to the large numbers of exquiaxed grains formed along molten pool boundaries on the XZ-plane. It can also be identified that the average misorientation angle on the XY-plane was lower than that of the XZ-plane. The misorientation angles on the XZ-plane concentrated around 35°-55°, while the misorientation angles on the XY-plane concentrated around 20°-40°. Besides, as shown in Table 1, the XY-plane possesses a higher fraction of LAGBs than the XZ-plane, which were 14.4% and 8.5%, respectively.

Fig. 6 shows pole figures and inverse pole figures for the Al-Mg-Sc-Zr specimen produced by SLM. A strong < 001 > texture along the building direction can be observed from the inverse pole figures as shown in Fig. 6b. This can also be confirmed in the pole figures as shown in Fig. 6a, where a < 001 > texture concentration along building direction was detected. The overall texture intensity can be provided by the texture index [1]:

$$Texture\ index = \int_{eulerspace} (f(g))^2 dg \quad (1)$$

Where f represents the texture orientation distribution, g represents the

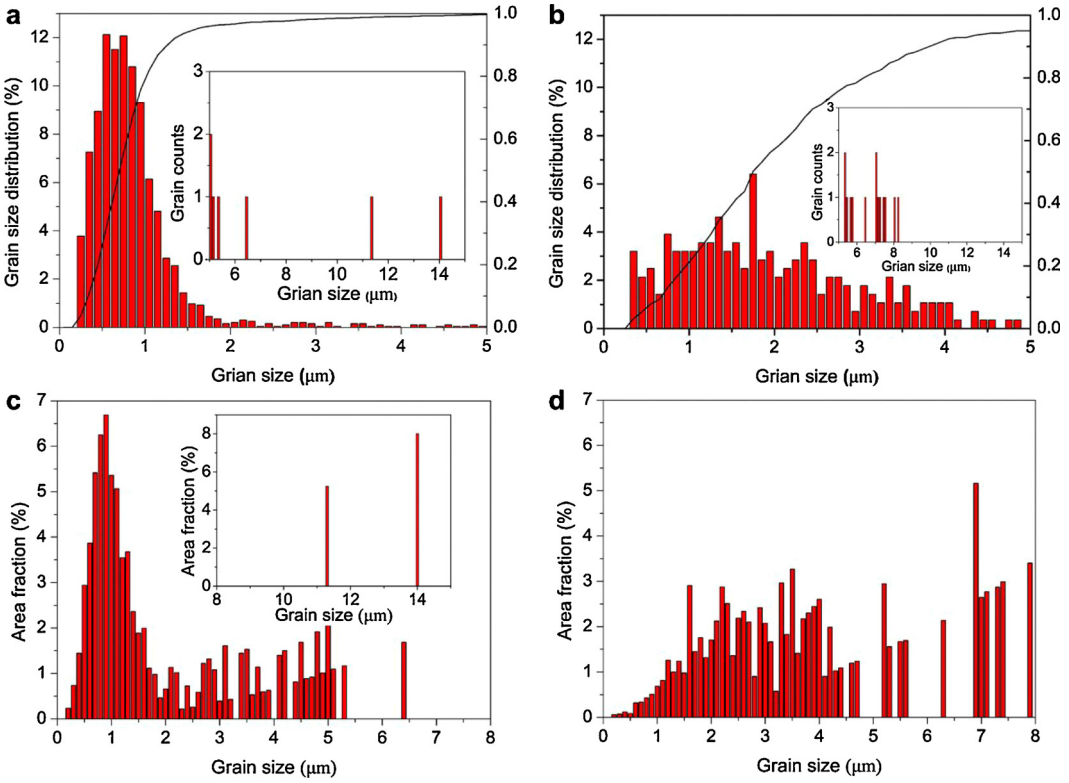

Fig. 4. Grain size distributions of SLM produced Al-Mg-Sc-Zr specimen on (a) and (c): XZ-plane; (b) and (d): XY-plane.

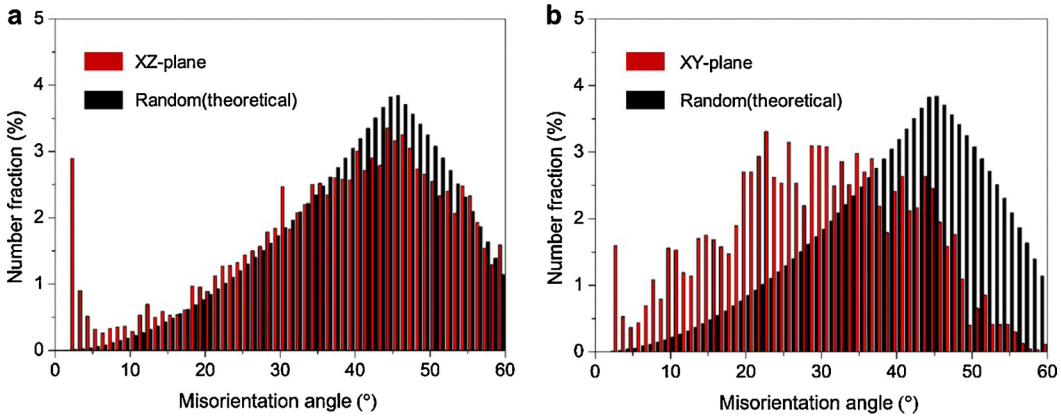

Fig. 5. Misorientation angle distribution of (a) XZ-plane and (b) XY-plane of SLM produced Al-Mg-Sc-Zr specimen.

Euler space coordinate system and $f(g)$ represents the orientation distribution function (ODF). Maximum intensity of the texture index of the SLM produced Al-Mg-Sc-Zr specimen was 1.97. For isotropic materials, this intensity of texture index is equal to unity [1]. Thus there are no apparent anisotropic mechanical properties of SLM produced Al-Mg-Sc-Zr alloy, which have been proved by Spierings [19] and Schmidtke [22]. However, the preferred orientation along (001) crystallographic direction significantly affects the surface condition on the XY- and XZ-planes of the SLM produced Al-Mg-Sc-Zr specimen. As shown in Fig. 3 (c) and (d), grains on the XZ-plane especially in the coarsen area were mostly oriented along (001) crystallographic direction whereas grains on the XY-plane exhibited a tendency of (111) crystallographic direction. Different crystal planes indicate different surface energies, which may considerably influence the corrosion behaviors on different planes of the SLM produced Al-Mg-Sc-Zr specimen.

3.2. Corrosion behaviors

Fig. 7 displays the variation of OCP values as a function of time for the XZ- and XY-planes of the SLM processed Al-Mg-Sc-Zr specimen tested in 3.5 wt.% NaCl solution. As time increased, OCP values for both planes kept shifting negative. OCP curve for the XZ-plane exhibited a considerate potential fluctuation, which probably related to the pitting corrosion. After tested for 10 h, stable potentials were obtained for the XY- and XZ-planes. The stabilized OCP values for the XZ-plane (i.e. -1126 ± 14 mV) was lower than that of the XY-plane (i.e. -875 ± 19 mV). All data were reproduced three times as summarized in Table 2. Generally, OCP values represent the integral and overall electrochemical behavior of the tested surface. A higher OCP value indicates a better corrosion resistance. Thus, according to the OCP tests, it is reasonable to consider a better corrosion resistance for the XY-plane of the SLM processed Al-Mg-Sc-Zr specimen compared to the XZ-plane.

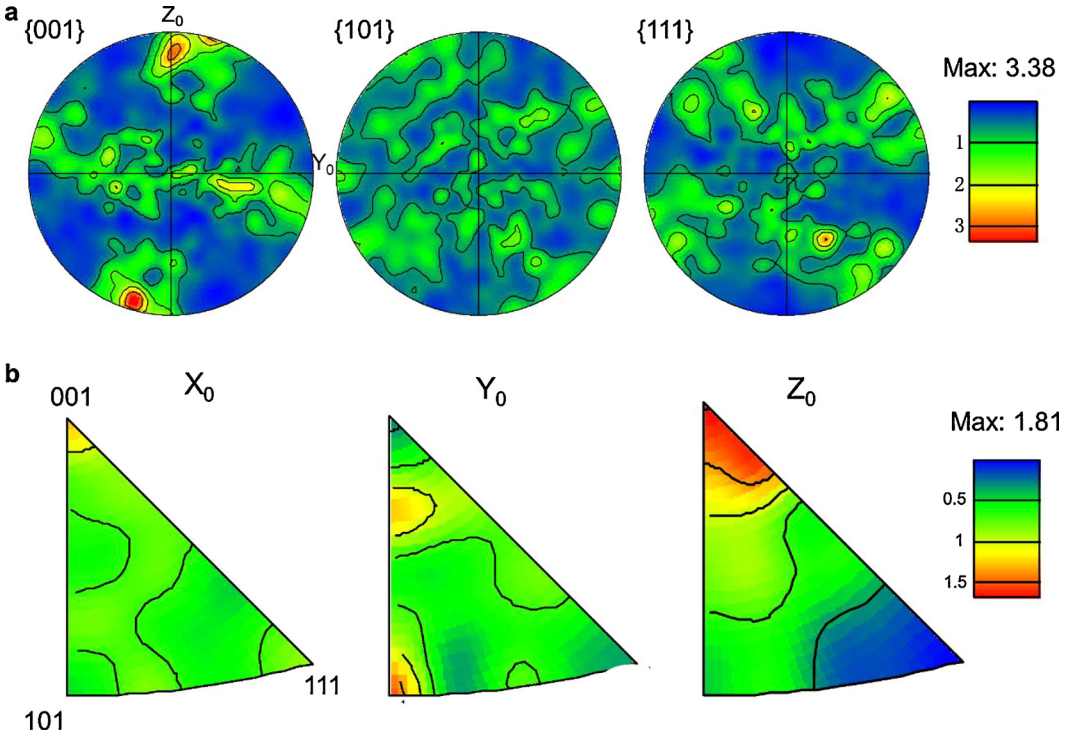

Fig. 6. (a) Pole figures (PF) and (b) inverse pole figures (IPF) of SLM produced Al-Mg-Sc-Zr specimen, showing a slight concentration of < 001 > crystallographic orientation along building direction. (X_0, Y_0 and Z_0 corresponding to the X, Y and Z direction as shown in Fig. 1c).

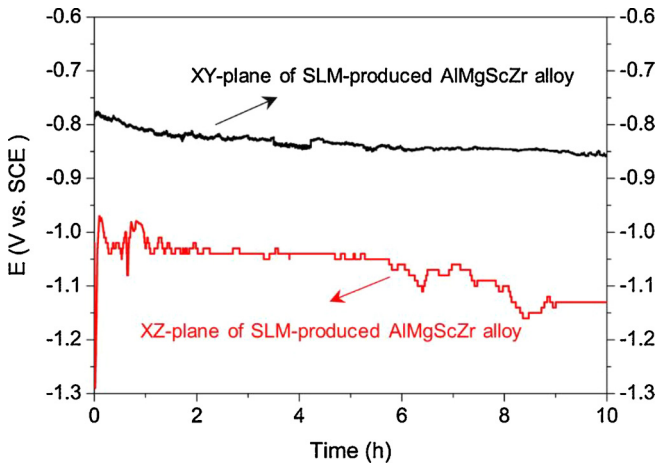

Fig. 7. Open circuit potential (OCP) as a function of time for XY- and XZ-planes of SLM produced Al-Mg-Sc-Zr specimen in 3.5 wt.% NaCl solution at room temperature.

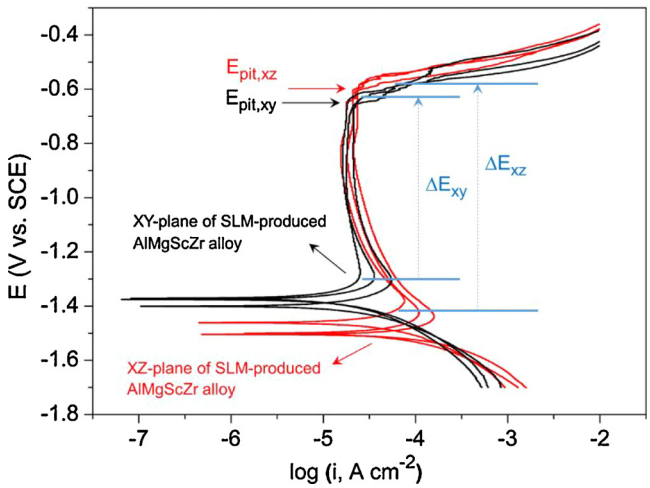

Fig. 8. Potentiodynamic curves for XY- and XZ-planes of SLM produced Al-Mg-Sc-Zr specimen in 3.5 wt.% NaCl solution at room temperature.

Fig. 8 presents polarization curves of the XZ- and XY-planes of the SLM produced Al-Mg-Sc-Zr specimen tested in 3.5 wt.% NaCl solution. Both XY- and XZ-planes exhibited apparent passive behaviors, which means passive films were formed on the surfaces. The XZ-plane displayed a broader potential range (ΔE_{xz}) of the passive process in comparison with that (ΔE_{xy}) of XY-plane. Based on a least square method, fitting parameters including corrosion current density(i_{corr}), cathodic Tafel slopes (β_c), anodic Tafel slope (β_a), pitting potential (E_{pit}) and polarization resistance (R_p) for the XY- and XZ-planes are provided in Table 3. A lower i_{corr} indicates a better corrosion resistance and a slower corrosion rate. As shown in Table 3, the i_{corr} for the XY-plane was 57.1 μA cm^{-2}, which was much lower than that of the XZ-plane (208.9 μA cm^{-2}). Meanwhile, the XY-plane exhibited a higher value of R_p than the XZ-plane, which were 38.75 × 10^2 Ω* cm^2 and 23.45 × 10^2

Table 2
Finally stabilized open circuit potential values for XY- and XZ-planes of SLM produced Al-Mg-Sc-Zr specimen after tested in 3.5 wt.% NaCl solution for 10 h. (each plane were tested for three times for data reproducibility)

Tested planes	First repeatability test	Second repeatability test	Third repeatability test	average
XZ-plane	−1.140 V	−1.112 V	−1.131 V	−1.127 V
XY-plane	−0.894 V	−0.883 V	−0.856 V	−0.877 V

Table 3
Fitting results of polarization curves for XY- and XZ-planes of SLM produced Al-Mg-Sc-Zr specimen in 3.5 wt.% NaCl solution. i_{corr}: corrosion current density, β_a: anodic Tafel slope, β_c: cathodic Tafel slope, E_{pit}: pitting potential and R_p: polarization resistance.

Specimens	i_{corr} (μA cm^{-2})	β_a (V/dec)	$-\beta_c$ (V/dec)	E_{pit} (V)	R_p (Ω* cm^2)
XZ-plane	289.5	2.646	4.269	−0.583	24.53 × 10^2
	190.2	1.353	4.991	−0.591	24.33 × 10^2
	147.2	0.861	4.695	−0.592	21.49 × 10^2
Average value	208.9	1.620	4.652	−0.589	23.45 × 10^2
Std-Dev	59.5	0.753	0.296	0.004	1.39 × 10^2
XY-plane	67.1	0.118	4.759	−0.623	7.46 × 10^2
	41.2	0.535	5.652	−0.631	51.58 × 10^2
	63.1	0.987	5.239	−0.635	57.23 × 10^2
Average value	57.1	0.547	5.217	−0.630	38.75 × 10^2
Std-Dev	11.3	0.355	0.365	0.005	22.25 × 10^2

Ω* cm^2, respectively. Thus it is reasonable to consider a better corrosion resistance for the XY-plane of the SLM produced Al-Mg-Sc-Zr specimen compared to the XZ-plane. However, as a key electrochemical parameter to evaluate pitting initiation susceptibility, the pitting potential (E_{pit}) for the XY-plane (i.e. -623 ± 6.0 mV) was slightly lower than that of the XZ-plane (i.e. -587 ± 4.5 mV). Generally, a higher E_{pit} indicates a better pitting corrosion resistance. As such, a comparison between the E_{pit} values of the XY- and XZ-planes suggested that it is slightly easier for the XY-plane of the SLM produced Al-Mg-Sc-Zr specimen to initiate pits compared to the XZ-plane. This observation was a little opposite to the conclusion obtained above, where the XY-plane possesses a better corrosion resistance than the XZ-plane. In other words, the XY-plane of the SLM produced Al-Mg-Sc-Zr specimen exhibited a better corrosion resistance in comparison with the XZ-plane in spite of a slightly lower pitting resistance in 3.5 wt.% NaCl solution.

EIS measurements were conducted to analyze surface conditions on the XY- and XZ-planes of the SLM produced Al-Mg-Sc-Zr specimen in the 3.5 wt.% NaCl solution. Fig. 9a-c show Nyquist and Bode plots of the XY- and XZ-planes of the SLM produced Al-Mg-Sc-Zr specimen. The characteristics frequencies were also marked out in the Nyquist plot. Based on the Nyquist plot shown in Fig. 9a, two apparent capacitive arcs were obtained for both XY- and XZ-planes. The radiuses of the loops of the XY-plane were significantly larger than the XZ-plane, suggesting a better corrosion resistance on the XY-plane. From the bode plots shown in Fig. 9b, two peaks were generated both for the XY- and XZ-planes, which included one peak (phase angles close 70-80°) at middle frequencies and another small peak (phase angles close 20-40°) at low frequencies. Accordingly, as shown in Fig. 9d, an equal circuit model with two time constants was applied to fitting the EIS data of the XY- and XZ-planes of the SLM produced Al-Mg-Sc-Zr specimen in 3.5 wt.% NaCl solution. In the equivalent circuit, R_s represents the solution resistance; CPE_1 is the capacitance of intact anodic film; R_f expresses the film resistance on the surface; CPE_2 reflects the capacitance of interface electric double layer and R_{ct} refers to the charge transfer resistance. Here, in order to evaluate the value of the double layer capacitance represented by a CPE, the Brug's formula can be used as follows [28,29]:

$$C = [Q(R_e^{-1} + R_{ct}^{-1})^{(\alpha-1)}]^{1/\alpha} \quad (2)$$

Where R_e is the electrolyte resistance. Table 4 summarized the fitting results of the EIS data. Chi-squared values (χ^2) represent the fitting quality, which ranged from 2.47 × 10^{-4} to 8.52 × 10^{-4}, suggesting a good agreement between the EIS data and the fitting results. The fitting result of R_f for the XY-plane was 43.88 kΩ cm^2, much higher than that of the XZ-plane (7.12 kΩ cm^2). As such, the XY-plane of the SLM produced Al-Mg-Sc-Zr specimen exhibited a better corrosion resistance than the XZ-plane, which was in accord with the experiment results of OCP tests and polarization tests. Besides, the corresponding capacitance can be obtained based on the CPE value of the film, which can be used to evaluate the film thickness. The effective capacitance (C_{eff})

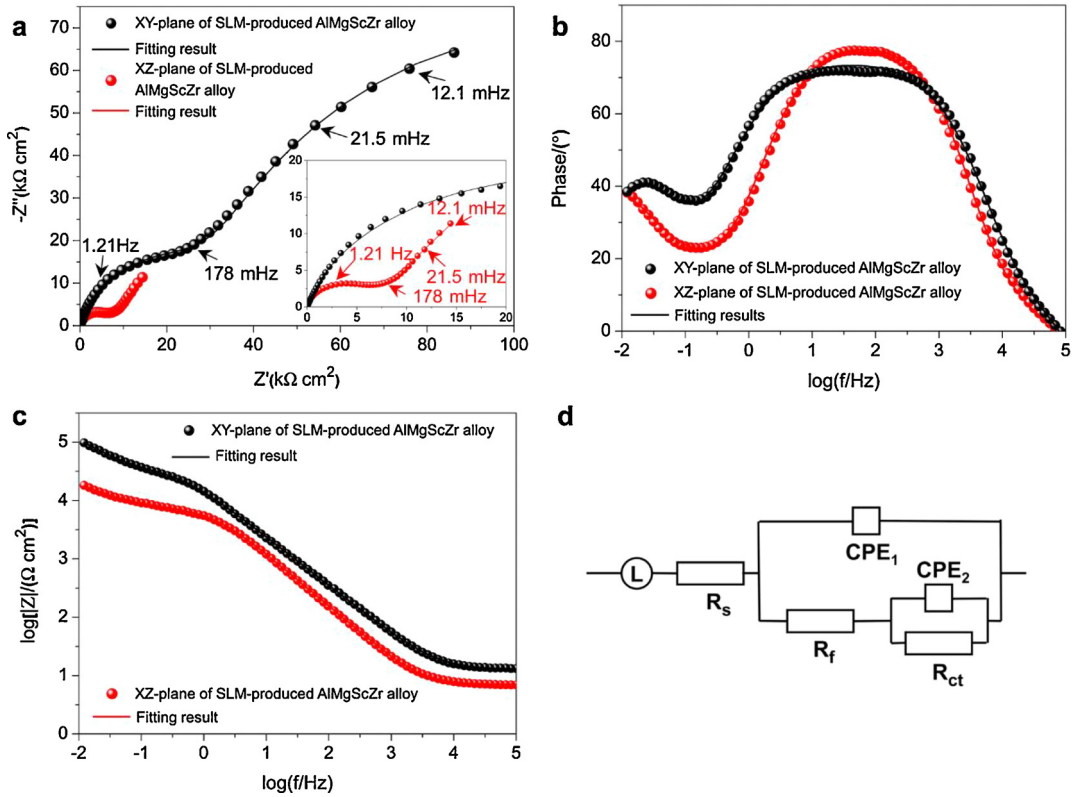

Fig. 9. EIS measurements of XY- and XZ- planes of the SLM produced AlMgScZr alloy in 3.5 wt.% NaCl solution at room temperature: (a) Nyquist plots; (b) and (c) Bode plots; (d) equivalent circuit model.

Table 4
The fitting parameters of EIS measurements for the XY- and XZ-planes of SLM produced Al-Mg-Sc-Zr specimen in 3.5 wt.% NaCl solution at room temperature. χ^2: Chi-squared values, R_f: film resistance on the surface, CPE_1: film capacitance, R_{ct}: charge transfer resistance, and CPE_2: double layer capacitance respectively.

Specimens	$\chi^2 \times 10^{-4}$ Chi-squared values	R_f (kΩ cm^2)	$CPE_1 \times 10^{-6}$ (F $cm^{-2}s^{n-1}$)	n_1	R_{ct} (kΩ cm^2)	$CPE_2 \times 10^{-4}$ (F $cm^{-2}s^{n-1}$)	n_2
XZ-plane	3.72	7.25	18.9	0.90	272.3	3.69	0.63
	2.83	5.94	21.91	0.80	282.5	4.76	0.80
	2.47	8.16	19.9	0.80	197.3	4.42	0.80
Average	3.01	7.12	20.24	0.83	250.7	4.29	0.75
Std-Dev	0.52	0.91	1.25	0.05	37.99	0.44	0.08
XY-plane	5.44	39.78	12.94	0.83	161.7	0.86	0.86
	8.52	51.24	14.74	0.81	212.2	0.59	0.85
	6.69	40.62	12.56	0.80	167.2	1.02	0.80
Average	6.88	43.88	13.41	0.81	180.3	0.82	0.84
Std-Dev	1.31	5.22	0.95	0.02	22.62	0.18	0.03

associated with the CPE can be expressed as [30]:

$$C_{eff} = Q^{1/\alpha} R_f^{(1-\alpha)/\alpha} \quad (3)$$

Where α is the CPE parameters and R_f expresses the film resistance on the surface. The capacitance is also related to film thickness d_{eff} according to [30]:

$$C_{eff} = \frac{\varepsilon \varepsilon_0}{d_{eff}} \quad (4)$$

Where ε represents the dielectric constant and ε_0 is the permittivity of vacuum, which is 8.8542×10^{-14} F/cm. For Al-Mg-Sc-Zr alloy tested in NaCl solution, the oxide is assumed to be Al_2O_3 and $\varepsilon = 9.1$ [31]. Thus the values of d_{eff} for the XY- and XZ-planes of the Al-Mg-Sc-Zr specimen can be evaluated, which are 5.9 Å for XZ-plane and 6.8 Å for XY-plane. Although this derivation may be cannot accurately obtain the actual film thickness, it can get a general trend that the oxide film formed on the XY-plane was thicker than the-XZ plane.

Morphologies on the XY- and XZ-planes of the SLM produced Al-Mg-Sc-Zr specimen after polarization tests in 3.5 wt.% NaCl solution were observed and provided in Fig. 10. Fig. 10a and c show the corrosion morphologies on the XY- and XZ-planes at a low magnification, respectively. As shown in Fig. 10a, after polarization test, the track-by-track configuration of molten pool boundaries can be identified clearly on the XY-plane, indicating pits were formed along molten pool boundaries. A similar feature was also obtained for the XZ-plane (Fig. 10c), where pits distributed along straight lines. These lines were vertical to the building direction and related to the molten pool boundaries formed layer-by-layer. Comparing the corrosion morphologies on the XY- and XZ-planes, it is obvious that the corroded area on the XY-plane was larger than that of the XZ-plane. Typical morphologies of the pits on the XY- and XZ-planes are shown in Fig. 10b and d at a high magnification, respectively. Pits on both planes showed crystallographic configuration. Besides, pits on the XY-plane were wide and shallow, while pits on the XZ-plane were deep. The wide corroded area on the XY-plane indicated it is easy for the XY-plane to initiate pits, but the limited depth of the pits suggested it is not easy for these pits to further propagate. This is well consistence with the results of the electrochemical tests, which showed an inferior pitting resistance but better corrosion resistance for the XY-plane. In contrast, less but deep pits on the XZ-plane indicated it is difficult for XZ-plane to initiate pits, but once the passive film broke down and pits formed, it propagated quickly and formed deep holes. These deep pits on the XZ-plane are easier to cause component failure during engineering application compared to the wide and shallow pits formed on the XY-plane. As such, pits on the XZ-plane are more harmful than that on the XY-plane.

3.3. Passive film composition

In order to further reveal the corrosion mechanisms of the SLM produced Al-Mg-Sc-Zr alloy. Compositions of the passive film formed on the surface of the SLM produced Al-Mg-Sc-Zr specimen in 3.5 wt.% NaCl solution at room temperature after potentiostatic polarization for 10 h were performed using XPS. Peaks of Al, Mg, C, O are identified in Fig. 11a. Peaks of Al, Mg and O are further provided in Fig. 11(b)-(c). The atomic percentage observed by the XPS in the surface of the of the passive film were 53.6% for C, 2.84% for Mg, 11.69% for Al and 31.86% for O. As shown in Fig. 11b and c, there were no metallic state of Al and Mg can be identified in the passive film. Al was identified in two chemical states, as indicated by the peaks at 74.5 eV and 75.7 eV, which related to Al_2O_3 and $Al(OH)_3$, respectively [32]. The content of Al_2O_3 was higher than $Al(OH)_3$. Similar to Al, Mg 2p ionization was also separated into two constituent peaks, including metallic Mg (45.3 eV) and MgO (50.8 eV) [33]. O 1s peaks presented in three chemical states (Fig. 11d). One peak at 531.3 eV related to Al_2O_3, which was related to the metallic oxides. The second peak at 532.2 eV represented $Al(OH)_3$, which was corresponded to the metallic hydroxides in the passive film, and the third peak at 533.6 eV related to H_2O [34]. As such, the constitutions of the passive film formed on the surface of the SLM produced Al-Mg-Sc-Zr specimen in 3.5 wt.% NaCl solution mainly consisted of metallic oxides and metallic hydroxides of Al and metallic oxides of Mg. Considering the low intensity of Mg peaks as shown in Fig. 11a and the limited content of Mg in initial powders, the majority of the passive film were Al_2O_3 and $Al(OH)_3$. Reactions for the formation of the passive films are proposed as follows:

The preferential cathodic and anodic reaction are shown in Eqs. (5) and (6), respectively.

$$O_2 + 2H_2O + 4e\text{-} \rightarrow 4OH\text{-} \quad (5)$$

$$Al \rightarrow Al^{3+} + 3e\text{-} \quad (6)$$

Then the Al^{3+} reacted with (OH)- to form metallic hydroxides.

$$Al^{3+} + 3(OH)\text{-} \rightarrow Al(OH)_3 \quad (7)$$

As the reaction proceeded, $Al(OH)_3$ was unstable and could be quickly dehydrated to Al_2O_3.

$$2Al(OH)_3 \rightarrow Al_2O_3 + 3H_2O \quad (8)$$

Thus compositions of the passive film formed on the surface of the SLM produced Al-Mg-Sc-Zr specimen in 3.5 wt.% NaCl solution mainly consisted of Al_2O_3 and $Al(OH)_3$.

4. Discussion

In this work, electrochemical tests were conducted in 3.5 wt.% NaCl solution to investigate the corrosion behaviors on the XY- and XZ-planes of the SLM produced Al-Mg-Sc-Zr specimen. Results indicated the XY-plane exhibited a superior corrosion resistance compared to the XZ-plane. To reveal the reasons for this anisotropic corrosion behavior, several factors including precipitations, grain size distribution, misorientation angle and crystallographic orientation were discussed in detail in the following sections.

4.1. The influence of precipitations on corrosion behavior

Precipitation plays an important role in the corrosion behavior of precipitation strengthened aluminum alloys. Sc and Zr modified Al-Mg alloy is mainly strengthened by $Al_3(Sc,Zr)$ precipitations. These precipitations are slightly cathodic with respect to the surrounding α-Al matrix, which facilitates the dissolution of the matrix adjacent to the $Al_3(Sc,Zr)$ particle during corrosion tests [35,36]. There are two kinds of $Al_3(Sc,Zr)$ precipitations in Al-Mg-Sc-Zr alloy, which consist of primary $Al_3(Sc,Zr)$ formed during solidification process and secondary

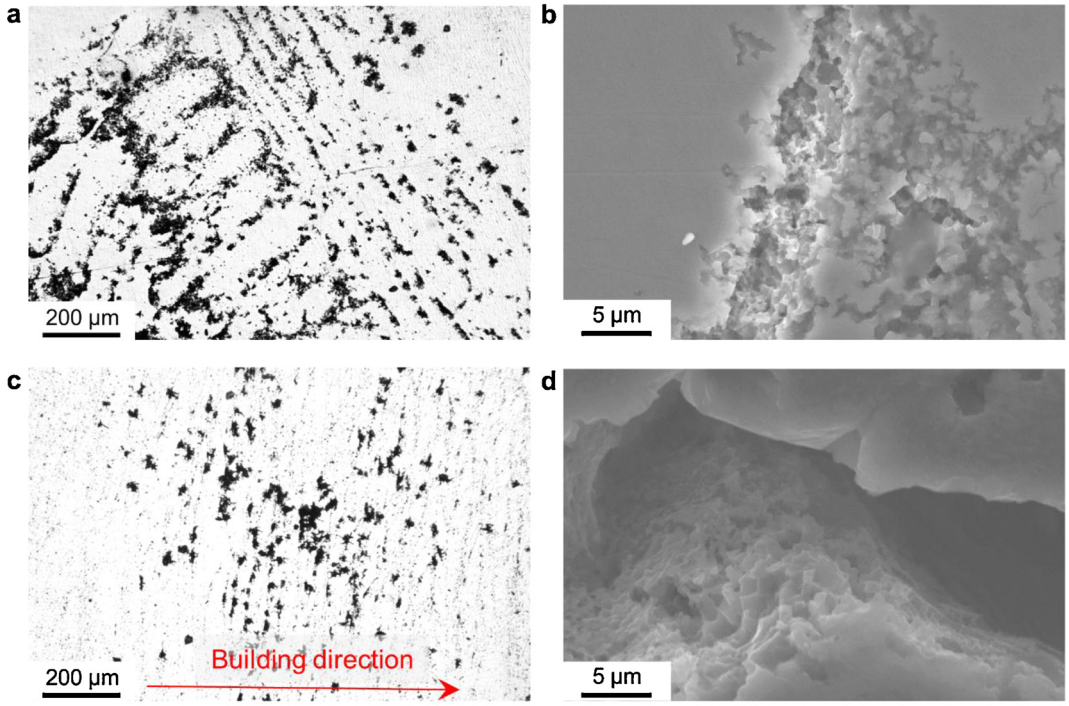

Fig. 10. Surface morphology of SLM produced Al-Mg-Sc-Zr specimen after polarization tests in 3.5 wt.% NaCl solution: (a) optical image and (b) SEM image for XY-plane, (c) optical image and (d) SEM-image for XZ-plane.

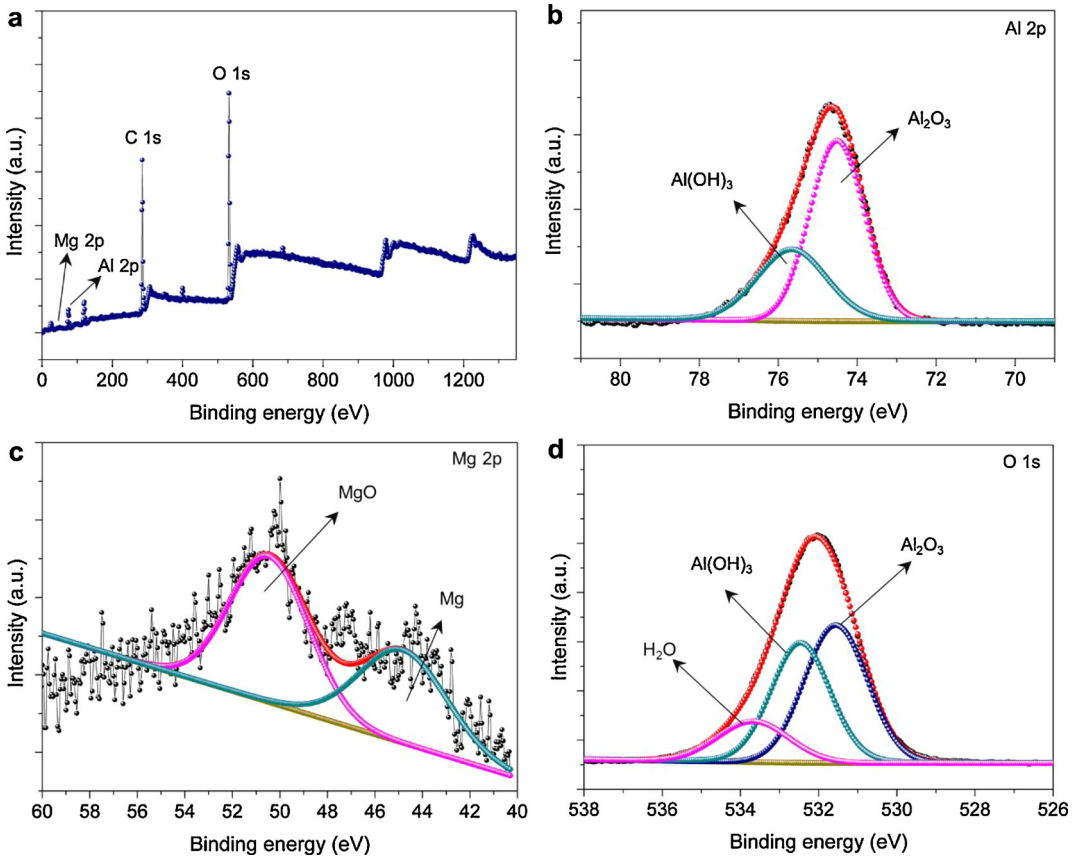

Fig. 11. High resolution XPS of the passive film formed on the surface of SLM produced Al-Mg-Sc-Zr specimen after immersion test in 3.5wt.% NaCl solution for 10 h: (a) Survey results, (b) Al-2p, (c) Mg 2p and (d) O 1s.

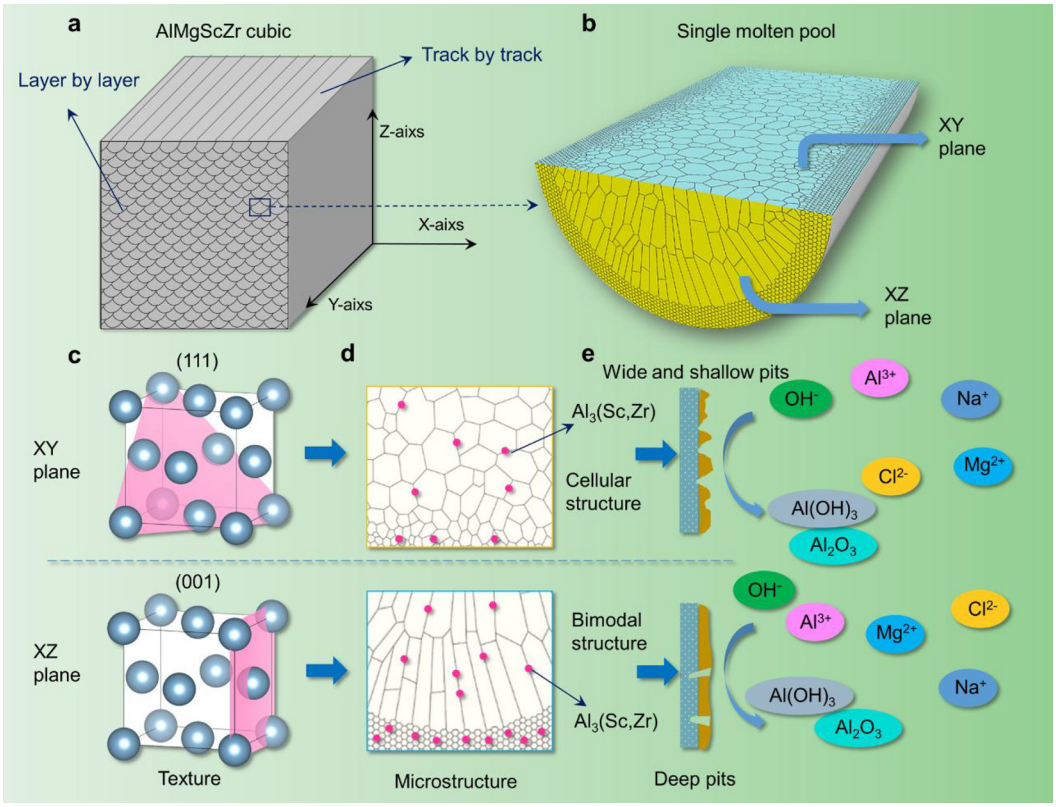

Fig. 12. Schematic of different microstructures and corrosion mechanisms on XY- and XZ- planes of SLM produced Al-Mg-Sc-Zr specimen. (a) Schematic diagram of different molten pool boundary densities on XY- and XZ- planes. (b) Schematic of the grain size distribution of a single molten pool, showing a bimodal microstructure on XZ-plane and a cellular grain feature on XY-plane. (c) Schematic of different crystallographic orientations, which consist of a (111) preferred oritentation on XY-plane and a (001) preferred oritentation on XZ-plane. (d) Schematic represents different precipitation distributions of XY- and XZ- planes, where red point represent the $Al_3(Sc,Zr)$ precipitation. (e) Schematic of different corrosion mechanisms on XY- and XZ- planes.

$Al_3(Sc,Zr)$ generated during the post heat treatment process. Generally, the secondary $Al_3(Sc,Zr)$ precipitations are uniformly distributed in the matrix with nano-size about 5 ~ 10 nm [37]. These secondary precipitations can not act as electrochemical units and resultantly do little contributions to the corrosion behaviors due to their nano-size [38]. Thus it is the primary $Al_3(Sc,Zr)$ precipitations that influence the corrosion resistance. For SLM produced Al-Mg-Sc-Zr alloy, primary $Al_3(Sc,Zr)$ precipitations are mainly distributed at the fine grain area along the molten pool boundaries (Fig. 2b), which also has been proved by Spierings and Shi [19,26]. However, due to the unique layer-by-layer characteristic of the SLM process, molten pool boundary densities on the XY- and XZ-planes are significantly different. As shown in Fig. 2a and illustrated in Fig. 12a, molten pool boundary density on the XZ-plane is considerately higher than that on the XY-plane, leading to primary $Al_3(Sc,Zr)$ precipitations exposed on the XZ-plane are much higher than that on the XY-plane. These particles can facilitate the breakdown of the $Al(OH)_3/Al_2O_3$ passive film formed on the surface and accelerate the failure of the surrounding α-Al matrix. As a result, the different precipitation behaviors on the XY- and XZ-planes may be one of the key factors to the anisotropic corrosion resistance of the SLM processed Al-Mg-Sc-Zr alloy.

4.2. The influence of grain size distribution on corrosion behavior

Grain size is another important factor to influence the corrosion behavior. The relationship between grain size and corrosion resistance relates to specific material and environment. For aluminum alloy, the majority of works suggested that the corrosion rate tends to decrease as grain size decreases [39,40]. The decreased grain size leads to the enhancement of the grain boundary density, which makes the surface more reactive. Irregular arrangement of atoms and unevenly distributed elements at grain boundaries are the main reasons accelerating the reaction [41]. Thus the passive film grows faster when the grain size is smaller (grain boundary density is higher), leading to a better pitting resistance. A Hall-Petch kind of correlation between i_{corr} and average grain size d was further provided by Ralston [39]:

$$i_{corr} = a + bd^{-\frac{1}{2}} \quad (9)$$

Where a and b are constants depending on the material and corrosive environment. It is found that b is a positive value in a non-passivating environment but a negative value in a passivating environment [42]. For SLM produced Al-Mg-Sc-Zr alloy, typical passive processes were observed both on the XY- and XZ-planes in polarization tests (Fig. 8). The composition of this passive film was further confirmed as $Al(OH)_3$ and Al_2O_3 in the XPS analysis (Fig. 11). Thus b is negative for SLM produced Al-Mg-Sc-Zr alloy in 3.5 wt.% NaCl solution, and the corrosion resistance should be enhanced as the grain size decrease. The average grain size for the XZ-plane is significantly lower than that of the XY-plane as shown in Table 1, which are 0.87 μm and 2.17 μm, respectively. As such, the pitting resistance of the XZ-plane should be better than the XY-plane. Besides, recent work revealed that grain size distribution can also act as a key role in the corrosion behavior especially for materials with uneven grain size distribution [42]. A decreased corrosion resistance was proved for a bimodal microstructure in a passivating environment. For the XZ-plane of the SLM produced Al-Mg-Sc-Zr alloy, a typical bimodal microstructure with fine grains along the molten pool boundaries and coarse grains in the center of the molten pools was obtained as shown in Fig. 2b and Fig. 3a. While for the XY-plane, grains are mainly cellular structure with less difference in grain size. These different grain size distributions on XY- and XZ-planes

are further illustrated in Fig. 12b and d. The bimodal microstructure is understood to enhance the strength and ductility, but tends to decrease the corrosion resistance of the XZ-plane.

4.3. The influence of misorientation on corrosion behavior

Prior studies indicated that grain boundary misorientation can affect the corrosion resistance of Al-Mg alloys. Low angle grain boundaries (LAGBs, grain orientation < 15°) have been proved to possess a better corrosion resistance [43]. As shown in Fig. 5, the average misoritentation angle on the XY-plane is lower than that on the XZ-plane. The fraction of LAGBs on the XY-plane is 14.4%, higher than that on the XZ-plane, which is 8.5%. In such cases, it is reasonable to consider a better corrosion resistance for the XY-plane. However, the grain boundary density on the XZ-plane is much higher than that of the XY-plane of SLM produced Al-Mg-Sc-Zr specimen as shown in Table 1, which are 15.87 mm^{-1} and 26.72 mm^{-1}, respectively. Thus the total length of LAGBs on XZ-plane (i.e. 0.37 mm) is higher than the XY-plane (i.e. 0.23 mm). As such, grain boundary density (i.e. grain size) plays a more important role in the corrosion resistance on the different planes of SLM produced Al-Mg-Sc-Zr alloy than the grain boundary misorientation. The influence of grain boundary misorientation on the anisotropic corrosion resistance of SLM produced Al-Mg-Sc-Zr alloy is limited.

4.4. The influence of crystallographic orientation on corrosion behavior

Crystallographic orientation is also an important factor to influence the electrochemical behavior of metal materials. No general relationship between crystallographic orientation and corrosion behavior were obtained based on an overview of literatures [44–46]. The results are highly related to the materials and corrosive environments. For aluminum alloy, the pitting susceptibility in chloride solution ranks in this order: (111) > (110) > (001) [47,48]. This is attributed to the different surface energies of (111), (110) and (100) crystal planes of aluminum alloy, where surface energies of (111) and (100) planes are 939 ± 30 erg/cm^2 and 1081 ± 30 erg/cm^2, respectively [49]. This conclusion was also supported by Soltis [50] and Yasuda [51], who indicate more metastable pits will initial on the (111) plane compared to other crystal planes of aluminum alloy during corrosion. In addition, pit formation on (111) surface involves the removal of the (100) subsurface atoms, while pit formation on (001) surface involves the dissolution of the more tightly bound (111) subsurface atoms [47]. This is another reason for the better pitting resistance on the (001) crystal plane of aluminum alloys. For SLM produced Al-Mg-Sc-Zr alloy, there is a (001) preferred orientation along building direction as shown in Fig. 6. The texture index is low (i.e. 1.97), indicating no apparent texture was formed in the SLM produced Al-Mg-Sc-Zr alloy. This is consistent with the isotropic mechanical properties of SLM produced Al-Mg-Sc-Zr alloy [19,22]. This slight orientation concentration has little influence on the mechanical properties, but significantly affects the surface conditions on different planes. As shown in Fig. 3c and d, the grain orientation on the XY-plane was mainly (001) especially for the coarsen area in the center of the molten pool. While compared to the XZ-plane, the grain orientation for the XY-plane exhibited a (111) tendency. As such, it is easier for the XY-plane to initial pits than XZ-plane, which leads to the lower value of E_{pit} for the XY-plane. This is also consistent with the observation of the corrosion morphology, where more pits were formed on the XY-plane.

In conclusion, the anisotropic corrosion behavior of SLM produced Al-Mg-Sc-Zr alloy is mainly attributed to the precipitation distribution, grain size distribution and crystallographic orientation. The key influencing factors are schematically shown in Fig. 12, and the mechanisms for the anisotropic corrosion resistance of SLM produced Al-Mg-Sc-Zr alloy in 3.5 wt.% NaCl solution are proposed as follows. At a very early stage of the corrosion process, passive films consist of $Al(OH)_3$ and Al_2O_3 are formed both on the XY- and XZ-planes. Due to the refined grain size and the high grain boundary density, the XZ-plane is more reactive than the XY-plane, which leads to a faster formation of an oxide film on the XZ-plane. In addition, the (001) crystallographic orientation on the XZ-plane makes the XZ-plane more difficult to initial pits. While the (001) crystallographic orientation on the XY-plane promotes the initiation of pits. Thus pits are first formed on the XY-plane, and that is the reason for the lower value of E_{pit} of the XY-plane as shown in Fig. 8. Once the passive films break down and pits formed, $Al_3(Sc,Zr)$ precipitations play the predominant role in corrosion process. These intermetallic particles serve as local cathodes and significantly facilitate the dissolution of the surrounding α-Al matrix. The amount of precipitations exposed on the XZ-plane is much higher than that on the XY-plane due to the higher molten pool boundary density as shown in Fig.2. The bimodal microstructure of the XZ-plane also promotes the propagation of pits. As such, the pit propagation on the XZ-plane is much quickly than the XY-plane. Thus wide and shallow pits are formed on the XY-plane, while less but deep pits are generated on the XZ-plane (Fig. 12e). All the pits tend to initial at the molten pool boundary due to the high grain boundary density and the aggregation of $Al_3(Sc,Zr)$ precipitations (Fig. 2b). For engineering application, deep pits formed on the XZ-plane are more harmful and are more likely to cause component failure. Thus it is better to make the XY-plane of SLM produced Al-Mg-Sc-Zr alloy to be the serving surface during engineering application. Furthermore, it should be pointed out that corrosion behavior is a very complicated process, and it involves many influencing factors [52]. The internal stress, dislocation density, chemical composition and the interface of precipitation may also play important roles in the corrosion behavior of SLM produced Al-Mg-Sc-Zr alloy. The detailed relationship between these factors and the corrosion behavior of SLM produced Al-Mg-Sc-Zr alloy should be investigated systematically in our future work.

5. Conclusion

In this work, corrosion behaviors on different planes of SLM produced Al-Mg-Sc-Zr alloy were investigated. The results of this work are summarized as follows:

- Microstructures of SLM produced Al-Mg-Sc-Zr alloy are different on XY- and XZ-planes. The molten pool boundary density of the XZ-plane is much higher than that on the XY-plane due to the layer-by-layer manufacturing characteristic of the SLM process. $Al_3(Sc,Zr)$ precipitations are preferred to generate along molten pool boundaries, making the precipitations exposed on the XZ-plane are higher than the XY-plane. Besides, the average grain size on the XZ-plane is lower than the XY-plane, which are 0.87 μm and 2.17 μm, respectively. XZ-plane exhibits a bimodal grain feature consisting of columnar grains in molten pool center and equiaxed grains along the molten pool boundary. While for the XY-plane, grains are mainly cellular structure with less grain size differences. A slightly (001) preferred crystallographic orientation was detected along building direction, making grains on XY-plane are mainly oriented along (111) crystal orientation while for XZ-plane are mainly oriented along (001) crystal orientation.
- Electrochemical measurements show that the XY-plane possesses higher OCP value (-0.877 V), lower corrosion current density (57.1 μA cm^{-2}) and higher polarization resistance (43.88 kΩ cm^2) compared to the XZ-plane. Thus the XY-plane exhibits a better corrosion resistance than the XZ-plane. While the XZ-plane displays a better resistance for pitting initiation as a higher E_{pit} (-0.589 V) was obtained. Passive behavior was observed for both planes, and the compositions of the passive film are mainly Al_2O_3 and $Al(OH)_3$. After polarization tests, wide and shallow pits were formed on the XY-plane while less but deep pits were generated on the XZ-plane.
- A mechanism was proposed for the anisotropic corrosion behavior

of SLM produced Al-Mg-Sc-Zr alloy. At the early stage, passive film was quickly generated on the XZ-plane due to its refined grain size and high grain boundary density. The (111) crystallographic orientation on the XY-plane further makes the XY-plane easier to initial pits compared to (001) crystallographic orientation on the XZ-plane. Once the passive film is broken down, $Al_3(Sc,Zr)$ precipitations play a dominate role. These intermetallic particles acted as local cathodes and promoted the propagation of pits. Since the molten boundary density and the amount of precipitations on the XZ-plane are much higher than the XY-plane, pits on the-XZ plane propagated quickly and formed deep pits. While the propagation rate of pits on the XY-plane is much lower than the XZ-plane, but it is easier for XY-plane to initial new pits, thus pits on XY plane are wide and shallow.

Author contributions section

Dongdong Gu: Experiment design, development, funding and paper writing.
Han Zhang: Experiment development.
Donghua Dai: Experiment development.
Chenglong Ma: Experiment development.
Hongmei Zhang: Experimental development.
Yuxin Li: Experimental development.
Shuhui Li: Research discussion.

Data Availability

The raw/processed data required to reproduce these findings cannot be shared at this time as the data also forms part of an ongoing study.

Declaration of Competing Interest

This paper mainly focused on the anisotropic corrosion behavior of Al-Mg-Sc-Zr alloy processed by selective laser melting. We declare that we do not have any commercial or associative interest that represents a conflict of interest in connection with the work submitted

Acknowledgements

We are grateful for the financial support from National Natural Science Foundation of China (No. 51735005); National Key Research and Development Program “Additive Manufacturing and Laser Manufacturing” (Nos. 2016YFB1100101, 2018YFB1106302); National Natural Science Foundation of China for Creative Research Groups (Grant No. 51921003); The 15th Batch of “Six Talents Peaks” Innovative Talents Team Program “Laser Precise Additive Manufacturing of Structure-Performance Integrated Lightweight Alloy Components” (No. TD-GDZB-001); 2017 Excellent Scientific and Technological Innovation Teams of Universities in Jiangsu “Laser Additive Manufacturing Technologies for Metallic Components” funded by Jiangsu Provincial Department of Education of China.

Appendix A. Supplementary data

Supplementary material related to this article can be found, in the online version, at doi:https://doi.org/10.1016/j.corsci.2020.108657.

References

[1] L. Thijs, K. Kempen, J.P. Kruth, J. Van Humbeeck, Fine-structured aluminium products with controllable texture by selective laser melting of pre-alloyed AlSi10Mg powder, Acta Mater. 61 (2013) 1809–1819, https://doi.org/10.1016/j.actamat.2012.11.052.
[2] Q. Yan, M. Wang, Y. Zhang, B. Song, L. Zhang, J. Zhang, Y. Shi, Amorphous alloy strengthened stainless steel manufactured by selective laser melting: Enhanced strength and improved corrosion resistance, Scr. Mater. 148 (2018) 20–23, https://doi.org/10.1016/j.scriptamat.2018.01.016.
[3] D. Gu, X. Rao, D. Dai, C. Ma, L. Xi, K. Lin, Laser additive manufacturing of carbon nanotubes (CNTs) reinforced aluminum matrix nanocomposites: Processing optimization, microstructure evolution and mechanical properties, Addit. Manuf. 29 (2019) 100801, , https://doi.org/10.1016/j.addma.2019.100801.
[4] M. Cabrini, S. Lorenzi, T. Pastore, S. Pellegrini, E.P. Ambrosio, F. Calignano, D. Manfredi, M. Pavese, P. Fino, Effect of heat treatment on corrosion resistance of DMLS AlSi10Mg alloy, Electrochim. Acta. 206 (2016) 346–355, https://doi.org/10.1016/j.electacta.2016.04.157.
[5] D. Wang, Y. Wang, Y. Yang, J. Lu, Z. Xu, S. Li, K. Lin, D. Zhang, Research on design optimization and manufacturing of coating pipes for automobile seal based on selective laser melting, J Mater Process Tech 273 (2019) 116227.
[6] E.O. Olakanmi, R.F. Cochrane, K.W. Dalgarno, A review on selective laser sintering / melting (SLS / SLM) of aluminium alloy powders : Processing, microstructure, and properties, J. Prog. Mater. Sci. 74 (2015) 401–477, https://doi.org/10.1016/j.pmatsci.2015.03.002.
[7] D. Wang, C. Song, Y. Yang, Y. Bai, Investigation of crystal growth mechanism during selective laser melting and mechanical property characterization of 316L stainless steel parts, Mater Design 100 (2016) 291–299, https://doi.org/10.1016/j.matdes.2016.03.111.
[8] D. Wang, Y. Yang, R. Liu, D. Xiao, J. Sun, Study on the designing rules and processability of porous structure based on selective laser melting (SLM), J Mater Process Tech 213 (2013) 1734–1742, https://doi.org/10.1016/j.jmatprotec.2013.05.001.
[9] N. Kang, P. Coddet, L. Dembinski, H. Liao, C. Coddet, Microstructure and strength analysis of eutectic Al-Si alloy in-situ manufactured using selective laser melting from elemental powder mixture, J. Alloys Compd. 691 (2017) 316–322, https://doi.org/10.1016/j.jallcom.2016.08.249.
[10] K.G. Prashanth, S. Scudino, J. Eckert, Defining the tensile properties of Al-12Si parts produced by selective laser melting, Acta Mater. 126 (2017) 25–35, https://doi.org/10.1016/j.actamat.2016.12.044.
[11] H. Zhang, H. Zhu, T. Qi, Z. Hu, X. Zeng, Selective laser melting of high strength Al-Cu-Mg alloys: Processing, microstructure and mechanical properties, Mater. Sci. Eng. A. 656 (2016) 47–54, https://doi.org/10.1016/j.msea.2015.12.101.
[12] W. Reschetnik, J.-P. Brüggemann, M.E. Aydinöz, O. Grydin, K.-P. Hoyer, G. Kullmer, H.A. Richard, Fatigue crack growth behavior and mechanical properties of additively processed EN AW-7075 aluminium alloy, Procedia Struct, Integr. 2 (2016) 3040–3048, https://doi.org/10.1016/j.prostr.2016.06.380.
[13] S.Z. Uddin, L.E. Murr, C.A. Terrazas, P. Morton, D.A. Roberson, R.B. Wicker, Processing and characterization of crack-free aluminum 6061 using high-temperature heating in laser powder bed fusion additive manufacturing, Addit. Manuf. 22 (2018) 405–415, https://doi.org/10.1016/j.addma.2018.05.047.
[14] K.E. Knipling, D.N. Seidman, D.C. Dunand, Ambient- and high-temperature mechanical properties of isochronally aged Al-0.06Sc, Al-0.06Zr and Al-0.06Sc-0.06Zr (at.%) alloys, Acta Mater. 59 (2011) 943–954, https://doi.org/10.1016/j.actamat.2010.10.017.
[15] E.A. Marquis, D.N. Seidman, Coarsening kinetics of nanoscale Al3Sc precipitates in an Al-Mg-Sc alloy, Acta Mater. 53 (2005) 4259–4268, https://doi.org/10.1016/j.actamat.2005.05.025.
[16] K.V. Yang, Y. Shi, F. Palm, X. Wu, P. Rometsch, Columnar to equiaxed transition in Al-Mg(-Sc)-Zr alloys produced by selective laser melting, Scr. Mater. 145 (2018) 113–117, https://doi.org/10.1016/j.scriptamat.2017.10.021.
[17] R. Li, M. Wang, T. Yuan, B. Song, C. Chen, K. Zhou, P. Cao, Selective laser melting of a novel Sc and Zr modified Al-6.2 Mg alloy: Processing, microstructure, and properties, Powder Technol. 319 (2017) 117–128, https://doi.org/10.1016/j.powtec.2017.06.050.
[18] M. Wang, R. Li, T. Yuan, C. Chen, L. Zhou, H. Chen, M. Zhang, S. Xie, Microstructures and mechanical property of AlMgScZrMn - A comparison between selective laser melting, spark plasma sintering and cast, Mater. Sci. Eng. A. 756 (2019) 354–364, https://doi.org/10.1016/j.msea.2019.04.060.
[19] A.B. Spierings, K. Dawson, K. Kern, F. Palm, K. Wegener, SLM-processed Sc- and Zr-modified Al-Mg alloy: Mechanical properties and microstructural effects of heat treatment, Mater. Sci. Eng. A. 701 (2017) 264–273, https://doi.org/10.1016/j.msea.2017.06.089.
[20] A.B. Spierings, K. Dawson, T. Heeling, P.J. Uggowitzer, R. Schäublin, F. Palm, K. Wegener, Microstructural features of Sc- and Zr-modi fi ed Al-Mg alloys processed by selective laser melting, Mater. Des. 115 (2017) 52–63, https://doi.org/10.1016/j.matdes.2016.11.040.
[21] R. Li, H. Chen, H. Zhu, M. Wang, C. Chen, T. Yuan, Effect of aging treatment on the microstructure and mechanical properties of Al-3.02Mg-0.2Sc-0.1Zr alloy printed by selective laser melting, Mater. Des. 168 (2019) 107668, , https://doi.org/10.1016/j.matdes.2019.107668.
[22] K. Schmidtke, F. Palm, A. Hawkins, C. Emmelmann, Process and mechanical properties: Applicability of a scandium modified Al-alloy for laser additive manufacturing, Phys. Procedia. 12 (2011) 369–374, https://doi.org/10.1016/j.phpro.2011.03.047.
[23] N. Dai, L. Zhang, J. Zhang, X. Zhang, Q. Ni, Y. Chen, Distinction in corrosion resistance of selective laser melted Ti-6Al-4V alloy on different planes, Corrosion Science 111 (2016) 703–710.
[24] J. Røyset, N. Ryum, Scandium in aluminum alloys, Int. Mater. Rev. 50 (2005) 19–44, https://doi.org/10.1179/174328005X14311.
[25] J.R. Croteau, S. Griffiths, M.D. Rossell, C. Leinenbach, C. Kenel, V. Jansen, D.N. Seidman, D.C. Dunand, N.Q. Vo, Microstructure and mechanical properties of Al-Mg-Zr alloys processed by selective laser melting, Acta Mater. 153 (2018) 35–44, https://doi.org/10.1016/j.actamat.2018.04.053.
[26] Y. Shi, K. Yang, S.K. Kairy, F. Palm, X. Wu, P.A. Rometsch, Effect of platform

temperature on the porosity, microstructure and mechanical properties of an Al–Mg–Sc–Zr alloy fabricated by selective laser melting, Mater. Sci. Eng. A. 732 (2018) 41–52, https://doi.org/10.1016/j.msea.2018.06.049.
[27] M. Orłowska, E. Ura-Bińczyk, L. Olejnik, M. Lewandowska, The effect of grain size and grain boundary misorientation on the corrosion resistance of commercially pure aluminium, Corros. Sci. 148 (2019) 57–70, https://doi.org/10.1016/j.corsci.2018.11.035.
[28] G.J. Brug, A.L.G. Van Den Eeden, M.S. Rehbach, J.H. Sluyters, The analysis of electrode impedances complicated by the presence of a constant phase element, J Electroanal Chem. 176 (1984) 275–295.
[29] P. Córdoba-torres, T.J. Mesquita, O. Devos, B. Tribollet, V. Roche, R.P. Nogueira, On the intrinsic coupling between constant-phase element parameters α and Q in electrochemical impedance spectroscopy, Electrochim. Acta. 72 (2012) 172–178.
[30] B. Hirschorn, M.E. Orazem, B. Tribollet, V. Vivier, I. Frateur, M. Musiani, Determination of effective capacitance and film thickness from constant-phase-element parameters, Electrochim. Acta. 55 (2010) 6218–6227.
[31] V. Shekar, M. Campbell, S. Akella, Towards automated optoelectrowetting on dielectric devices for multi-axis droplet manipulation, 2013 IEEE International Conference on Robotics and Automation, Karlsruhe, 2013, pp. 1439–1445.
[32] S.E. Potts, G. Dingemans, C. Lachaud, Plasma-enhanced and thermal atomic layer deposition of $Al2O_3$ using aluminum precursor, J. Vac. Sci. Technol. A. 2 (2012) 1–12, https://doi.org/10.1116/1.3683057.
[33] J.R.R Jr, D.M. Bickham, C.J. Powell, The NIST X-ray Photoelectron Spectroscopy Database 19 (1992), pp. 241–246.
[34] D. Kong, X. Ni, C. Dong, L. Zhang, C. Man, J. Yao, K. Xiao, X. Li, Heat treatment effect on the microstructure and corrosion behavior of 316L stainless steel fabricated by selective laser melting for proton exchange membrane fuel cells, Electrochim. Acta. 276 (2018) 293–303, https://doi.org/10.1016/j.electacta.2018.04.188.
[35] J. Wloka, S. Virtanen, Influence of scandium on the pitting behaviour of Al-Zn-Mg-Cu alloys, Acta Mater. 55 (2007) 6666–6672, https://doi.org/10.1016/j.actamat.2007.08.021.
[36] M.K. Cavanaugh, N. Birbilis, R.G. Buchheit, F. Bovard, Investigating localized corrosion susceptibility arising from Sc containing intermetallic Al3Sc in high strength Al-alloys, Scr. Mater. 56 (2007) 995–998, https://doi.org/10.1016/j.scriptamat.2007.01.036.
[37] J. Taendl, A. Orthacker, H. Amenitsch, G. Kothleitner, C. Poletti, Influence of the degree of scandium supersaturation on the precipitation kinetics of rapidly solidified Al-Mg-Sc-Zr alloys, Acta Mater. 117 (2016) 43–50, https://doi.org/10.1016/j.actamat.2016.07.001.
[38] Z. Ahmad, A. Ul-Hamid, A.A. B.j, The corrosion behavior of scandium alloyed Al 5052 in neutral sodium chloride solution, Corros. Sci. 43 (2001) 1227–1243, https://doi.org/10.1016/S0010-938X(00)00147-5.
[39] K.D. Ralston, N. Birbilis, C.H.J. Davies, Revealing the relationship between grain size and corrosion rate of metals, Scr. Mater. 63 (2010) 1201–1204, https://doi.org/10.1016/j.scriptamat.2010.08.035.
[40] K.D. Ralston, D. Fabijanic, N. Birbilis, Effect of grain size on corrosion of high purity aluminium, Electrochim. Acta. 56 (2011) 1729–1736, https://doi.org/10.1016/j.electacta.2010.09.023.
[41] X. Gong, Y. Li, Y. Nie, Z. Huang, F. Liu, L. Huang, L. Jiang, H. Mei, Corrosion behaviour of CoCrMo alloy fabricated by electron beam melting, Corros. Sci. 139 (2018) 68–75, https://doi.org/10.1016/j.corsci.2018.04.033.
[42] S. Gollapudi, Grain size distribution effects on the corrosion behaviour of materials, Corros. Sci. 62 (2012) 90–94, https://doi.org/10.1016/j.corsci.2012.04.040.
[43] R. Zhang, Y. Qiu, Y. Qi, N. Birbilis, A closer inspection of a grain boundary immune to intergranular corrosion in a sensitised Al-Mg alloy, Corros. Sci. 133 (2018) 1–5, https://doi.org/10.1016/j.corsci.2018.01.009.
[44] H. Jia, X. Feng, Y. Yang, Effect of crystal orientation on corrosion behavior of directionally solidified Mg-4 wt% Zn alloy, J. Mater. Sci. Technol. 34 (2018) 1229–1235, https://doi.org/10.1016/j.jmst.2017.06.009.
[45] R. Xin, Y. Luo, A. Zuo, J. Gao, Q. Liu, Texture effect on corrosion behavior of AZ31 Mg alloy in simulated physiological environment, Mater. Lett. 72 (2012) 1–4, https://doi.org/10.1016/j.matlet.2011.11.032.
[46] P.T. Brewick, N. Kota, A.C. Lewis, V.G. DeGiorgi, A.B. Geltmacher, S.M. Qidwai, Microstructure-sensitive modeling of pitting corrosion: Effect of the crystallographic orientation, Corros. Sci. 129 (2017) 54–69, https://doi.org/10.1016/j.corsci.2017.09.009.
[47] H. Krawiec, Z. Szklarz, Combining the Electrochemical Microcell Technique and the Electron Backscatter Diffraction method to study the electrochemical behaviour of polycrystalline aluminium in sodium chloride solution, Electrochim. Acta. 203 (2016) 426–438, https://doi.org/10.1016/j.electacta.2016.03.030.
[48] G.M. Treacy, C.B. Breslin, Electrochemical studies on single-crystal aluminium surfaces, Electrochim. Acta. 43 (1998) 1715–1720.
[49] J. Sch, P. Bohnen, M. Ho, Structure and dynamics at the Al(111)-surface, Surf Sci 324 (1995) 113–121.
[50] J. Soltis, Passivity breakdown, pit initiation and propagation of pits in metallic materials - Review, Corros. Sci. 90 (2015) 5–22, https://doi.org/10.1016/j.corsci.2014.10.006.
[51] M. Yasuda, F. Weinberg, D. Tromans, Pitting Corrosion of AI and AI-Cu Single Crystals, J. Electrochem. Soc. 137 (1990) 3708–3715.
[52] Z. Szklarska-Smialowska, Pitting corrosion of aluminum, Corros. Sci. 41 (1999) 1743–1767, https://doi.org/10.1016/S0010-938X(99)00012-8.